APP Template V1.70 Article id: ppcfab5144 Typesetter: MPS Date received by MPS: 28/10/2019 PE: MAC006894 CE: LE:

UNCORRECTED PROOF

IOP Publishing Plasma Physics and Controlled Fusion

Plasma Phys. Control. Fusion **00** (2019) 000000 (15pp)

Reduced model of high-Z impurity redeposition and erosion in tokamak divertor and its application to DIII-D experiments

J Guterl[1], W R Wampler[2], D Rudakov[3], T Abrams[4], H Q Wang[4], A G McLean[5] and P Snyder[4]

[1] Oak Ridge Associated Universities, United States of America
[2] Sandia National Laboratories, Albuquerque, NM, United States of America
[3] University of California San Diego, La Jolla, CA, United States of America
[4] General Atomics, San Diego, CA, United States of America
[5] Lawrence Livermore National Laboratory, Livermore, CA, United States of America

Received 23 July 2019, revised 16 October 2019
Accepted for publication 25 October 2019
Published DD MM 2019

Abstract

Q1 A reduced model of high-Z impurities erosion and redeposition is presented to analyze net erosion of tungsten material in divertor attached plasma conditions measured in DIII-D experiments. This reduced model is tailored to quantify the redeposition and the net erosion on high-Z material samples of sufficiently small dimensions to be considered exposed to uniform plasma conditions. For those uniform plasma conditions, the spatial distribution of redeposited high-Z impurities is well approximated by an analytical distribution characterized by a few parameters. The fraction of high-Z impurity eroding and redepositing on a material sample is then obtained by integrating this distribution across the material sample. The ratio of net erosion rates of tungsten measured experimentally from tungsten samples of different sizes exposed to the same attached plasma conditions are well reproduced with this reduced model. It is shown that uncertainties induced by radially non-uniform plasma conditions in experiments can be significantly reduced by exposing samples to high density divertor plasma. Several enhanced experimental setups are proposed to measure and compare net erosion rates from samples of various areas during a single plasma experiment.

Keywords: tungsten, redeposition, divertor, erosion

SQ1 (Some figures may appear in colour only in the online journal)

1. Introduction

Plasma-facing components (PFCs) in ITER and future fusion reactors will face significant particle and heat fluxes inducing material erosion, and thus limiting PFCs lifetime and core plasma performance due to contamination by high-Z impurities. The erosion of PFCs material is therefore a long-standing issue for Tokamaks and has been widely investigated for various material [1–3]. As the result of material gross erosion and impurity redeposition through the plasma, the net erosion of PFCs material ultimately determines the effective sources of impurity in tokamaks and the operational lifetime of PFCs.

Tungsten is currently the material of choice for divertor PFCs in future tokamaks, e.g. ITER [4]. Therefore, the net erosion of tungsten in divertor must be accurately predicted to guarantee the sustainability of divertor PFCs and plasma performances during diverted plasma operations [2]. In contrast to low-Z impurities like carbon or beryllium, the ionization of sputtered neutral tungsten impurities is fast enough to induce large prompt redeposition of sputtered particles when plasma temperature and density are high. Furthermore, the energy distribution of particles impinging on PFCs and inducing material sputtering strongly depends on divertor plasma conditions. Because of these strong dependencies of material sputtering and prompt redeposition on divertor plasma conditions, the net erosion of PFCs material might

 © 2019 IOP Publishing Ltd Printed in the UK

significantly differ whether the divertor plasma is attached or detached. The scope of this paper is limited to tungsten net erosion in presence of attached or partially detached divertor plasma conditions, when effects of background neutrals on impurity production and transport are negligible.

Tungsten gross erosion can be well monitored during plasma operations using spectroscopic measurements [5–7]. In contrast, measurements of tungsten net erosion and redeposition are obtained through the post-mortem analysis of material samples. Moreover, material samples are often analyzed after an integrated plasma campaign during which PFCs are exposed to various plasma conditions and plasma impurity contents [8–11]. Inferring the relationship between net erosion and plasma conditions from these experiments might be thus extremely complex.

A new experimental setup have been recently introduced and tested by Stangeby, Rudakov and Brooks in DIII-D to improve the experimental analysis of high-Z material net erosion [12–17]. Two high-Z material samples of different sizes were exposed to the same plasma conditions in the DIII-D lower divertor using DiMES [18, 19]. In these experiments, the amount of high-Z impurities sputtered and redeposited on a material sample is correlated to the characteristic size of the sample. Consequently, effects of impurity prompt redeposition on the net material erosion can be characterized through post-mortmem measurements of net erosion from samples of various sizes exposed to similar plasma conditions. The fraction of sputtered high-Z impurity, e.g. tungsten, which promptly redeposit may be large in attached or partially detached divertor plasma conditions [20, 21]. The experimental assessment of material net erosion in realistic divertor configurations provided by this experimental setup is thus critical to validate models of high-Z impurity prompt redeposition, and to predict the amount of high-Z impurities effectively penetrating into the scrape-off layer plasma.

Several features of high-Z material erosion and redeposition experiments conducted in DIII-D [7, 22] can be successfully reproduced with comprehensive modeling of impurity erosion, transport and redeposition in DIII-D SOL and divertor plasma. However, such modeling is usually complex, as it requires reconstructing the SOL plasma conditions in 2D and determining the sources of low-Z impurity (C, Be) in divertor. Low-Z impurities indeed induce large sputtering of high-Z material in attached divertor plasma conditions. Comprehensive modeling and interpretation of the aforementioned DIII-D experiments dedicated to measure net erosion of high-Z material [15, 16, 23] are thus rather complex. Nevertheless, Ding noticeably showed that the spatial profiles of the net erosion rates measured on the largest of the two samples are successfully reproduced with the ERO model [23].

To facilitate the interpretation and the analysis of those experiments, we introduce in this paper a reduced model of high-Z impurity erosion and redeposition on a material sample exposed to attached divertor plasma conditions. This model assumes that these plasma conditions are sufficiently uniform across the material sample in both toroidal and radial directions. Within this assumption, the spatial distribution of redeposited high-Z impurities can be well approximated by an analytical distribution characterized by a few parameters. The fraction of high-Z impurity eroding and redepositing on a material sample is then obtained from the integral of the distribution of impurities redeposited onto the material sample.

This reduced model is applied to analyze some of the aforementioned DIII-D experiments conducted to characterize tungsten net erosion [14–17]. During those experiments, several circular tungsten samples of various radii were exposed to attached plasma conditions. The net erosion rates corresponding to these plasma conditions were measured through post-morterm analysis of the tungsten samples. The ratio of the net erosion rates obtained from two samples of different size but exposed to the same plasma conditions predicted with the reduced model are in agreement with the ratio experimentally measured.

Furthermore, it is shown that uncertainties in the reduced model due to radially non-uniform plasma conditions can be significantly reduced when performing these experiments at high plasma density. Finally, several enhanced experimental setups are proposed to measure and compare net erosion rates from samples of various areas during a single plasma experiment in tokamak divertor.

For the sake of brevity, the reduced model introduced in this paper is only discussed and applied for tungsten impurities. This reduced model can be nevertheless easily transpose and applied to other high-Z impurities, such as molybdenum, provided that the fraction of promptly redeposited impurities remains large. It is noteworthy to mention that the reduced model introduced in this paper to analyze DIII-D experiments may not be straightforwardly applicable to estimate net erosion of high-Z material in tokamaks like ITER. However, characterizing the net erosion of high-Z material exposed to uniform plasma conditions as a function of few parameters may be extremely valuable to benchmark the modeling of key processes governing impurity prompt redeposition, and thus net erosion. For instance, tungsten prompt redeposition strongly depends on the ionization rates of neutral and low charge state tungsten impurities and on the width of the Chodura sheath [20], which is formed by the Debye sheath and a large magnetic pre-sheath [24]. Because these key parameters are virtually impossible to measure directly in experiments, robust analysis and modeling of material net erosion measurements in dedicated experiments are critical to validate the numerical estimations of these parameters [25, 26].

This paper is organized as follows. The reduced model of high-Z impurity erosion and redeposition is introduced in the section 2. Parameters characterizing the prompt redeposition of high-Z impurities in the reduced model are discussed in the section 3. The application of the reduced model to analyze tungsten redeposition experiments conducted in DIII-D is presented in the section 4. Finally, optimal size and shapes of material samples to measure net erosion of high-Z material are discussed in the section 5.

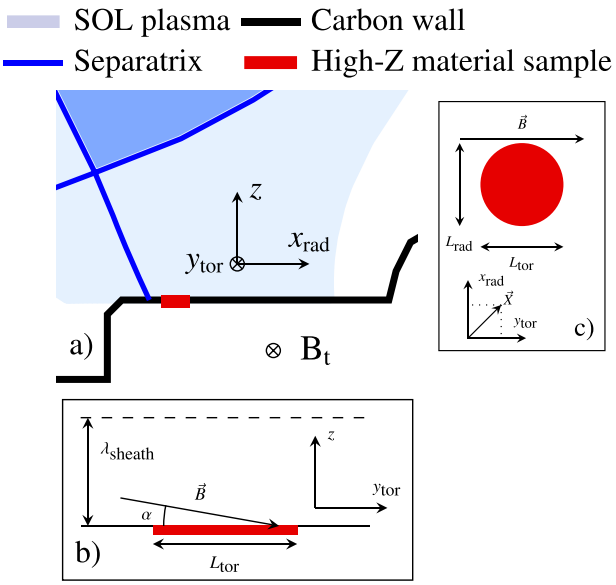

Figure 1. Sketch of high-Z material samples exposed to plasma in the lower divertor of DIII-D: poloidal view (a), tangential view (b) and horizontal view (c).

2. Reduced model of erosion and redeposition of high-Z impurities on material samples exposed to attached divertor plasma conditions

2.1. Redeposition of high-Z impurities in attached divertor plasma conditions

We consider here the erosion and redeposition of high-Z material exposed to attached plasma conditions typically found in DIII-D or similar tokamak divertors ($T_e = 10$–$40\,\mathrm{eV}$, $n_e = 10^{13}$–$10^{14}\,\mathrm{cm}^{-3}$). In those divertor plasma conditions, high-Z material is mainly sputtered by low-Z impurities and main plasma ions, and self-sputtering is negligible. The prompt redeposition of high-Z impurities, which corresponds to the redeposition of ionized impurities caused by their first gyration around the magnetic field near material surfaces [20, 27], is large in those plasma conditions. For instance, the fraction of promptly redeposited tungsten in those plasma conditions is typically larger than 90% [21].

Tungsten impurities which do not promptly redeposit can also redeposit when flowing along the magnetic fields in the scrape-off layer. These impurities exit and do not reenter immediately the electric sheath near the material surface due to the multiple ionizations of these impurities in higher charge states outside of the sheath [28]. The guiding center of these impurities is at a distance of the order of ρ_{imp} from the sheath entrance located at $z = \lambda_{sheath}$, where ρ_{imp} is the gyro-radius of a singly charged tungsten impurity, and λ_{sheath} is the width of the Chodura sheath. Furthermore, tungsten impurities which enter the Chodura sheath are likely to hit the material surface in the attached plasma conditions considered here [29]. Since magnetic field lines in standard tokamak divertor intersect divertor material surfaces at grazing incidence $0° < \alpha < 5°$ (figure 1(b)), non-promptly redeposited impurities, whose gyro-radius is smaller than ρ_{imp} due to multiple ionizations, redeposit in the toroidal direction at a typical distance $y_{tor} \gtrsim \frac{\rho_{imp}}{\alpha}$ from the sample.

Impurities eroded from a material sample without promptly redepositing on this same material sample can be thus ignored when the toroidal characteristic width L_{tor} of the material sample is short enough, i.e.

$$L_{tor} < \frac{\rho_{imp}}{\alpha}. \tag{1}$$

When the toroidal width of a material sample satisfies the condition 1, the redeposition of impurities on this sample can be assumed to be solely due to prompt redeposition. For instance, non-prompt redeposition of tungsten can be ignored for samples satisfying $L_{tor} \lesssim 1\,\mathrm{cm}$ for attached plasma conditions in the DIII-D divertor where $B \approx 2.25\,\mathrm{T}$ and $\alpha \approx 2°$. Since the prompt redeposition of tungsten is largely uniform in the toroidal direction (see section 3), toroidal profiles of tungsten net erosion should be symmetric with respect to the center of the material sample. Toroidal profiles of tungsten net erosion experimentally observed on circular tungsten samples of toroidal width $L_{tor} = 1\,\mathrm{cm}$ exposed to attached plasma conditions in DIII-D divertor [14, 23] exhibit a pattern relatively symmetric, in sharp contrast with toroidal profiles of deposited tungsten measured in the vicinity of the samples.

2.2. Fraction of high-Z impurities eroded and redeposited on a material sample exposed to uniform plasma conditions

Plasma temperature and density in tokamak divertor usually exhibit sharp radial variations, since the parallel transport of plasma along the magnetic field lines is much faster than the plasma transport across the magnetic field lines in the scrape-off layer. However, plasma conditions with broader radial profiles can be obtained for instance in the DIII-D lower divertor in reverse-B_t configuration [30]. The radial scale length of the plasma temperature and density in this configuration can be of the order of $\lambda_{rad} \sim 0.5$–$1\,\mathrm{cm}$ at the outer divertor target.

Material samples with a radial width L_{rad} inferior or comparable to the plasma temperature and density scale lengths ($L_{rad} \lesssim \lambda_{rad}$) can be therefore assumed to be exposed to uniform plasma conditions, as plasma are usually toroidally symmetric in tokamak configuration.

When the redeposition of low-Z impurity eroded in the vicinity of a material sample onto this material sample is negligible compared to the overall flux of impinging low-Z impurities, spatially uniform plasma conditions lead to spatially uniform fluxes and distributions of charge and energy of low-Z impurities and main plasma ions impinging onto the material sample. This condition is fulfilled when the toroidal width of the material sample is small compared to the toroidal distance at which low-Z impurity redeposit, which is usually the case when the condition (1) is fulfilled.

The sputtering of high-Z impurities induced by uniform flux and distribution of charge and energy of particles impinging onto high-Z material sample is also uniform. The term 'uniform' thus refers in this work to plasma conditions for which the gross erosion flux of high-Z impurity Γ_{ero}^{gross} can

be considered as uniform across the high-Z material sample, i.e.

$$L_{\mathrm{rad}}\frac{\partial \log(\Gamma_{\mathrm{ero}}^{\mathrm{gross}})}{\partial x_{\mathrm{rad}}} \ll 1 \text{ and } L_{\mathrm{tor}}\frac{\partial \log(\Gamma_{\mathrm{ero}}^{\mathrm{gross}})}{\partial y_{\mathrm{tor}}} \ll 1. \tag{2}$$

The fraction ξ_{redep} of high-Z impurities eroded and redeposited on a material sample exposed to uniform plasma conditions (conditions (2)) and of limited toroidal width (condition (1)) can be expressed as:

$$\xi_{redep}(S) = \beta_{\mathrm{redep}}\frac{\int_S\int_{S\cap\mathbb{R}^2}\hat{f}_{\mathrm{redep}}(\vec{X}+\vec{X}')\mathrm{d}\vec{X}\mathrm{d}\vec{X}'}{\int_S \mathrm{d}\vec{X}}. \tag{3}$$

S is the spatial domain of the sample, such that $\int_S \mathrm{d}\vec{X}$ is the area of the sample (figure 1(c)). $\hat{f}_{\mathrm{redep}}$ is the normalized spatial distribution of redeposited high-Z impurities,

$$\hat{f}_{\mathrm{redep}}(\vec{X}) = \frac{f_{\mathrm{redep}}(\vec{X})}{\int_{\mathbb{R}^2} f_{\mathrm{redep}}(\vec{X})\mathrm{d}\vec{X}}$$

with $\int_{\mathbb{R}^2} f_{\mathrm{redep}}(\vec{X})\mathrm{d}\vec{X} = \beta_{\mathrm{redep}}$. β_{redep} is the fraction of eroded high-Z impurities which promptly redeposit.

Using the expression (3), the average net erosion flux $\langle\Gamma_{\mathrm{ero}}^{\mathrm{net}}\rangle_S$ across a sample of surface S is given by

$$\langle\Gamma_{\mathrm{ero}}^{\mathrm{net}}\rangle_S = \frac{\int_S \Gamma_{\mathrm{ero}}^{\mathrm{net}}(\vec{x})\mathrm{d}\vec{x}}{\int_S \mathrm{d}\vec{x}} = \Gamma_{\mathrm{ero}}^{\mathrm{gross}}(1-\xi_{\mathrm{redep}}(S)). \tag{4}$$

The ratio $\Xi_{\mathrm{ero}}^{\mathrm{net}}$ of the average net erosion flux from two samples of surface S_1 and S_2 exposed to the same uniform plasma conditions is thus given by

$$\Xi_{\mathrm{ero}}^{\mathrm{net}}(S_2, S_1) = \frac{\langle\Gamma_{\mathrm{ero}}^{\mathrm{net}}\rangle_{S_2}}{\langle\Gamma_{\mathrm{ero}}^{\mathrm{net}}\rangle_{S_1}} = \frac{1-\xi_{\mathrm{redep}}(S_2)}{1-\xi_{\mathrm{redep}}(S_1)}. \tag{5}$$

The fraction ξ_{redep} of redeposited high-Z impurities does not explicitly depend on the gross erosion flux. $\Xi_{\mathrm{ero}}^{\mathrm{net}}$ is therefore only determined by the size and the shape of the material samples, and by the spatial distribution of promptly redeposited high-Z impurities. The comparison of $\langle\Gamma_{\mathrm{ero}}^{\mathrm{net}}\rangle$ measured on material samples of different size or shape, but exposed to the same uniform plasma conditions, thus provides an experimental characterization of the prompt redeposition of high-Z impurities.

It is noticeable that $\xi_{\mathrm{redep}}(S\to 0)\to 0$. The net and gross erosion fluxes of high-Z impurities eroded from samples smaller than the characteristic distance at which impurities redeposit are therefore comparable, as pointed out in [14, 16] and [23].

In the reduced model of high-Z impurity erosion and redeposition introduced in this section, $\Xi_{\mathrm{ero}}^{\mathrm{net}}$ only depends on the size and shape of the material samples, and on the spatial distribution f_{redep} of redeposited high-Z impurities. This distribution can be expressed in a simple analytical form as a function of a few parameters, as described in the next section.

3. Spatial distribution of promptly redeposited high-Z impurities

3.1. Numerical estimations of the spatial distribution of promptly redeposited high-Z impurities

The prompt redeposition of impurities is the result of the ionization and the motion of the sputtered impurities along and across the magnetic field in and out of the electric sheath. The ionization of neutral and low charge state high-Z impurities is usually fast in attached divertor conditions ($\tau_{\mathrm{iz}}\omega_c \ll 1$, with ω_c the impurity cyclotron frequency and τ_{iz} the characteristic ionization time). High-Z impurities are thus usually ionized multiple times during their first gyration around the magnetic field lines [28]. Because of the multiple ionizations of high-Z impurities during one gyration, the analytical description of the spatial distribution of redeposited impurities f_{redep} is cumbersome. In this work, f_{redep} is thus numerically evaluated for various plasma conditions.

The prompt redeposition of high-Z impurities occurs on a time scale $\tau_{\mathrm{prompt}} \sim \omega_c^{-1}$, which is usually much shorter than the time scale of collisions of high-Z impurities with plasma ions ($\nu_{\mathrm{coll}}\tau_{\mathrm{prompt}} \ll 1$ where ν_{coll} is the collision frequency), and effects of these collisions on prompt redeposition of high-Z impurities can be ignored. Collisions of high-Z impurity with neutrals are also neglected considering the low density of neutral particles in attached plasma conditions. Moreover, effects of the plasma electric field E_{plasma} outside of the sheath region on the impurity cross-field and parallel motion are also neglected $\left(\frac{4\pi^2 e}{M\omega_c^2}|E_{\mathrm{plasma}}| \ll 1\right)$, as well as the effects of anomalous cross field transport.

The prompt redeposition of high-Z impurities is strongly affected by the electric sheath near the surface [20]. The vertical scale length of the electric sheath in tokamak divertor is usually of the order of the main plasma ion gyroradius ρ_i when the magnetic field lines intersect the divertor material surface at grazing incidence [24, 31] (figure 1(b)). We consider in this work the spatial profile of the electric sheath potential $\phi(z) = -3\frac{k_b T_e}{e} \times e^{-\beta_{\mathrm{sheath}}\frac{z}{\lambda_{\mathrm{sheath}}}}$ calculated in [25] for $\alpha = 2°$, with $\lambda_{\mathrm{sheath}} \approx 5\rho_i$ and $\beta_{\mathrm{sheath}} = 4$. Values of ρ_i and $\lambda_{\mathrm{sheath}}$ are estimated assuming $T_i \approx T_e$, since experimental measurements or accurate theoretical estimations of T_i are usually difficult to obtain in tokamak divertor.

Sputtered high-Z impurities are assumed to be emitted from the material surface with an uniform azimuthal angular distribution, a cosine polar angular distribution and a Thompson energy distribution [32], as suggested for instance by simulations of tungsten sputtering by carbon with binary collision codes [33]. This energy distribution is characterized by the binding energy E_{b} and the cutoff energy E_{cutoff}. The ionization rates are taken from the ADAS database [34].

Within the assumptions described hereabove, the spatial distribution of promptly redeposited high-Z impurities—here tungsten—are calculated using the Monte-Carlo code ERO-D3D. ERO-D3D is an enhanced high computing performance version of the ERO code [35], which solves the equations of motion for impurity in 3D tokamak boundary plasma

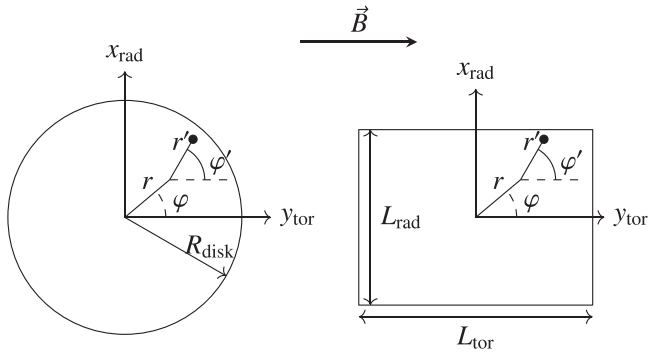

Figure 2. Polar coordinates for circular and rectangular material samples. y_{tor} is the toroidal direction and x_{radial} is the radial direction.

described in the original ERO manual [36]. Simulations are performed for various attached plasma conditions found in DIII-D divertor with $B = 2.25\,\mathrm{T}$, $\alpha = 2°$ and a surface binding energy for tungsten $E_b = 8.63\,\mathrm{eV}$. ERO-D3D is used here as a simple Monte-Carlo solver to model impurity ionization and redeposition in presence of electric and magnetic fields. Noticeably, the angle of incidence α does not affect significantly the spatial distribution of promptly redeposited particles at grazing incidence ($\alpha < 5°$). Two examples of the spatial distribution of promptly redeposited tungsten impurities calculated with ERO-D3D are shown in figures 3(a) and (d).

3.2. Analytical approximation of the spatial distribution of promptly redeposited high-Z impurities

The spatial distribution of redeposited high-Z impurities emitted from a point source is described by the probability density function $f_{redep}(r, \varphi)$, where r is the distance from the point source located at $r = 0$ and φ is the azimuthal angle relative to the toroidal axis (figure 2).

When the prompt redeposition of high-Z impurities is sufficiently large ($\beta_{redep} \gtrsim 0.7$), it can be shown that $\hat{f}_{redep}(r, \varphi)$ is well approximated by the product of two distributions

$$\hat{f}_{redep}(r, \varphi) \approx \begin{cases} \hat{f}_r^+(r)\hat{f}_\varphi(\varphi) & \text{for } 0 < \varphi < \pi \\ \hat{f}_r^-(r)\hat{f}_\varphi(\varphi) & \text{for } \pi < \varphi < 2\pi \end{cases}, \tag{6}$$

where

$$\hat{f}_r^\pm(r) = \gamma(r, \mu, \lambda_{redep}^\pm) \tag{7}$$

and

$$\hat{f}_\varphi(\varphi) = \frac{1}{2\pi}(1 + \eta_{asym}^{rad} \sin\varphi)$$

$\gamma(r, \mu, \lambda)$ is the gamma distribution

$$\gamma(r, \mu, \lambda) = \frac{r^{\mu-1}}{\Gamma(\mu)\lambda^\mu} e^{-\frac{r}{\lambda}}$$

characterized by the decay length λ and the shape parameter μ.

Two examples of the radial distributions of redeposited impurities are displayed in figures 3(b) and (e). The radial distribution in the positive radial direction ($0 < \varphi < \pi$) can differ significantly from the radial distribution of the particle redeposition in the negative radial direction ($\pi < \varphi < 2\pi$) due to the asymmetry of impurity redeposition across the magnetic field line in the radial direction x_{rad}, illustrated in figures 3(c) and (f). Hence the introduction of two different scale lengths λ_{redep}^- and λ_{redep}^+ characterizing the radial distribution of redeposited impurities in each region.

The asymmetry of the impurity redeposition in the radial direction, characterized by η_{asym}^{rad} in the expression of $\hat{f}_\varphi$, is caused by the ionizations of impurities outside of the the electric sheath. Let us consider for instance a magnetic field pointing in the positive toroidal direction ($B > 0$), as sketched in the figure 1. Impurities exiting the sheath with a negative radial velocity complete a larger gyration around the magnetic field before reentering into the sheath than impurities exiting the sheath with a positive radial velocity. As a consequence, impurities exiting the sheath with a negative radial velocity are more likely to be ionized out of the sheath and to not reenter the sheath than impurities exiting the sheath with a positive radial velocity. Impurities emitted with a positive radial velocity are thus more likely to redeposit than impurities emitted with a negative radial velocity.

In contrast, impurities are uniformly redeposited in the toroidal direction when the prompt redeposition is sufficiently large ($\beta_{redep} \gtrsim 0.7$), which is usually the case for high-Z impurities like tungsten in the attached plasma conditions considered in this work. Consequently, the toroidal profiles of tungsten net erosion are expected to be symmetric with respect to the center of the material sample.

3.3. Characteristic parameters describing the spatial distribution of redeposited tungsten

For a given impurity species, it can be shown that radial distributions of redeposited impurities can be well described by the distribution $\hat{f}_r$ (equation (7)) with a unique shape parameter μ for a large range of plasma conditions and cutoff energies. For instance, the radial distribution of redeposited tungsten can be well described by the distribution $\hat{f}_r$ with $\mu = 1.25$, as illustrated in figures 3(b) and (e). The characteristic lengths λ_{redep}^- and λ_{redep}^+ estimated from ERO-D3D simulations with $\mu = 1.25$ are shown in the figure 4 as a function of the plasma density for various plasma temperatures and cutoff energies. Corresponding values of η_{asym}^{rad} and β_{redep} are also plotted in figure 4.

The relationship between the radial asymmetry of impurity redeposition characterized by η_{asym}^{rad} and the ionization of impurities out of the sheath is illustrated by the similar evolution of η_{asym}^{rad} and $\beta_{z_{iz}>\lambda_{sheath}}$ with the plasma conditions in figure 4, where $\beta_{z_{iz}>\lambda_{sheath}}$ is the fraction of sputtered tungsten impurities which experience at least one ionization event out of the electric sheath.

As shown in figure 4, the parameters $\lambda_{redep}^\pm$, β_{redep} and η_{redep}^{rad} which characterize the spatial distribution of

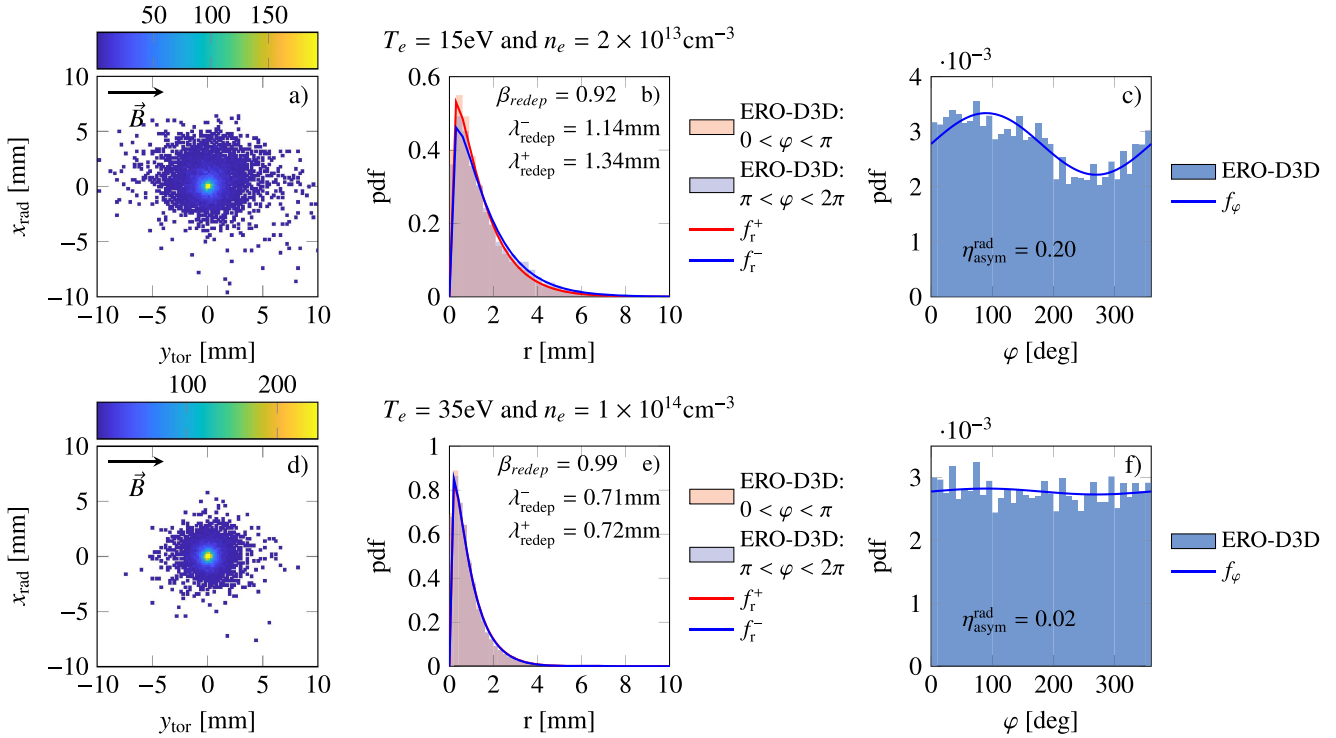

Figure 3. Examples of 2D, radial and azimuthal distributions of promptly redeposited tungsten calculated with ERO-D3D for low uniform plasma temperature and density (a)–(c) and high uniform plasma temperature and density (d)–(f), with $E_{\text{cutoff}} = 2T_e$. The energy and angular distributions of sputtered particles, the sheath model, the magnetic configuration and other assumptions used in ERO-D3D simulations are described in the section 3.1.

redeposited tungsten strongly depend on the cutoff energy E_{cutoff} of the energy distribution of impurities sputtered from material surface. The increase of E_{cutoff} strongly affects the magnitude of the radial asymmetry of the tungsten redeposition pattern, as more tungsten impurities ionize out of the sheath as their kinetic energy increase. A good approximation of E_{cutoff} is therefore necessary to accurately describe the redeposition distribution of high-Z impurities.

In the attached divertor plasma conditions considered in this work, the sputtering of high-Z impurities is mainly due to low-Z impurities (carbon in DIII-D). Assuming that $T_i \approx T_e$, the cutoff energy E_{cutoff} corresponding to the sputtering of high-Z impurities by low-Z impurities impinging on material surface at sub-keV energies can be then estimated by

$$E_{\text{cutoff}} \approx \frac{4\,mM}{(M+m)^2}\left(\frac{m+2M}{2m+2M}\right)^6 (3Z_{\text{low}}+1)T_e,$$

where m and Z_{low} are the mass and the charge of the low-Z impurities inducing sputtering of high-Z impurities of mass M [37]. Moreover, low-Z carbon impurities usually strike the DIII-D divertor surface in charge state 2+ and 3+ in attached plasma conditions [7], such that $E_{\text{cutoff}} \approx 1.3T_e - 1.9T_e$ for sputtered tungsten particles.

We have thus shown here that the spatial distribution of redeposited tungsten can be well approximated by an analytical distribution characterized by only a few parameters ($\lambda^{\pm}_{\text{redep}}$, $\eta^{\text{rad}}_{\text{asym}}$ and β_{redep}). Such description is remarkable considering that the redeposition of high-Z impurities is the result of various complex physics processes, i.e. multiple ionizations and motion in and out of the sheath of impurities emitted with distributed energy, polar angle and azimuthal angle. These few parameters can be handily used to analyze effects of plasma conditions on tungsten redeposition and net erosion.

For instance, the small variations of $\lambda^{\pm}_{\text{redep}}$, $\eta^{\text{rad}}_{\text{asym}}$ and β_{redep} at high plasma density (figure 4) indicate that varying plasma temperature and density will not significantly affect the spatial distribution of redeposited tungsten, provided that the plasma density remains large enough ($n_e > 5 \times 10^{13}\,\text{cm}^{-3}$). The characterization of the spatial distribution of redeposited high-Z impurities by only a few parameters may thus largely facilitate the design and the interpretation of erosion and redeposition divertor experiments, as illustrated in the next two sections.

4. Modeling and analysis of tungsten erosion and redeposition experiments with circular samples in DIII-D

Measurements of high-Z impurities were conducted in DIII-D using circular material samples [12, 14], as sketched in figure 1. The reduced model of high-Z impurity erosion and redeposition formed by the expressions (3) and (6) is used in this section to model and analyze tungsten erosion and redeposition from circular samples.

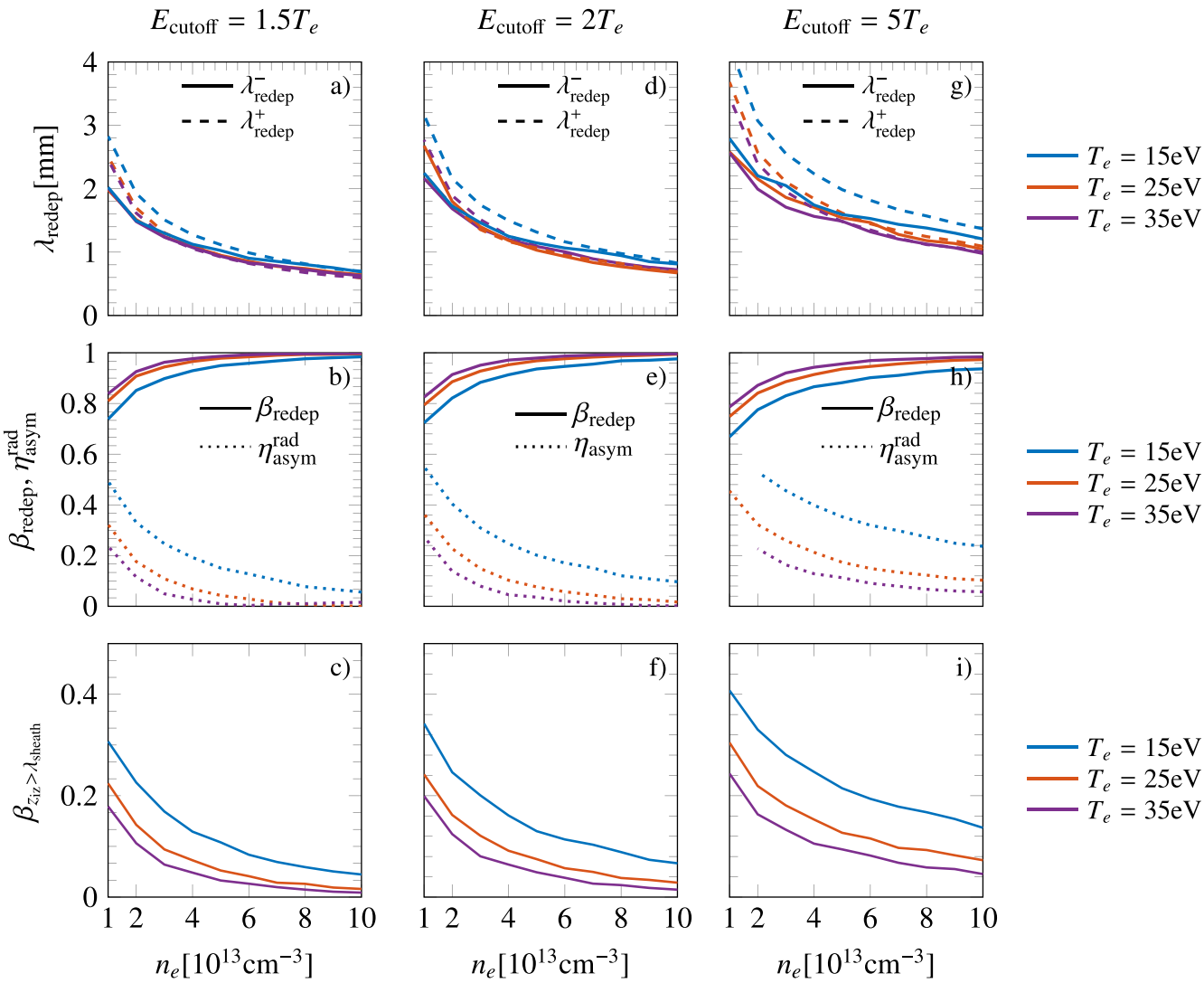

Figure 4. Characteristic parameters of the spatial distribution of redeposited tungsten calculated with ERO-D3D with uniform plasma conditions as a function of plasma temperature and density for $E_{\text{cutoff}} = 1.5T_e$ (a)–(c), $E_{\text{cutoff}} = 2T_e$ (d)–(f) and $E_{\text{cutoff}} = 5T_e$ (g)–(i). The shape parameter of the radial distribution of redeposited impurities is $\mu = 1.25$. The corresponding characteristic lengths $\lambda^{\pm}_{\text{redep}}$ are reported in the plots (a), (d), (g). The fraction β_{redep} of sputtered tungsten impurities which redeposit and the magnitude $\eta^{\text{rad}}_{\text{asym}}$ of the asymmetry of tungsten redeposition across the magnetic field lines are shown in the plots (b), (e), (h). The fraction $\beta_{z_{\text{iz}}>\lambda_{\text{sheath}}}$ of sputtered tungsten impurities which experience at least one ionization event out of the electric sheath is shown in the plots (c), (f), (i).

4.1. Fraction of high-Z impurities eroded and redeposited on circular material sample exposed to uniform plasma conditions

We consider here a material sample of circular shape and of radius R_{disk} (figure 2). Using the expression (3) and the redeposition distribution $\hat{f}_{\text{redep}}$ (equation (6)), the fraction $\xi_{\text{redep}}(\hat{R}_{\text{disk}})$ of impurities eroded and redeposited on the sample is given by

$$\xi_{\text{redep}}(R_{\text{disk}}) = \frac{\beta_{\text{redep}}}{2\pi^2 R^2_{\text{disk}}} \times \int_0^{R_{\text{disk}}}\int_0^{2\pi}\int_0^{2\pi}\int_0^{R_{\text{max}}} \hat{f}_{\text{redep}}(r', \varphi')\mathrm{d}r'\mathrm{d}\varphi'\mathrm{d}\varphi r\mathrm{d}r, \quad (8)$$

where $R_{\text{max}} = \sqrt{R^2_{\text{disk}} - r^2\sin^2(\varphi - \varphi')} - r\cos(\varphi - \varphi')$. The distribution $\hat{f}_{\text{redep}}(r', \varphi')$ is integrated in the expression (8) with respect to $\mathrm{d}r'$ and not $r'\mathrm{d}r'$. The integral of the distribution γ with respect to r' can be recast into a normalized form as

$$\int_0^{R_{\text{max}}} \gamma(r', \mu, \lambda)\mathrm{d}r' = \int_0^{\hat{R}_{\text{max}}} \gamma(\hat{r}', \mu, 1)\mathrm{d}\hat{r}',$$

where $\hat{R}_{\text{disk}} = \frac{R_{\text{disk}}}{\lambda}$, $\hat{r} = \frac{r}{\lambda}$ and $\hat{R}_{\text{max}} = \sqrt{\hat{R}^2_{\text{disk}} - \hat{r}^2\sin^2(\varphi - \varphi')} - \hat{r}\cos(\varphi - \varphi')$. ξ_{redep} can be then expressed as

$$\xi_{\text{redep}}(R_{\text{disk}}) = \chi_{\text{sym}}\left(\frac{R_{\text{disk}}}{\lambda^+_{\text{redep}}}\right) + \chi_{\text{sym}}\left(-\frac{R_{\text{disk}}}{\lambda^-_{\text{redep}}}\right) + \eta^{\text{rad}}_{\text{asym}}\left[\chi_{\text{asym}}\left(\frac{R_{\text{disk}}}{\lambda^+_{\text{redep}}}\right) - \chi_{\text{asym}}\left(-\frac{R_{\text{disk}}}{\lambda^-_{\text{redep}}}\right)\right], \quad (9)$$

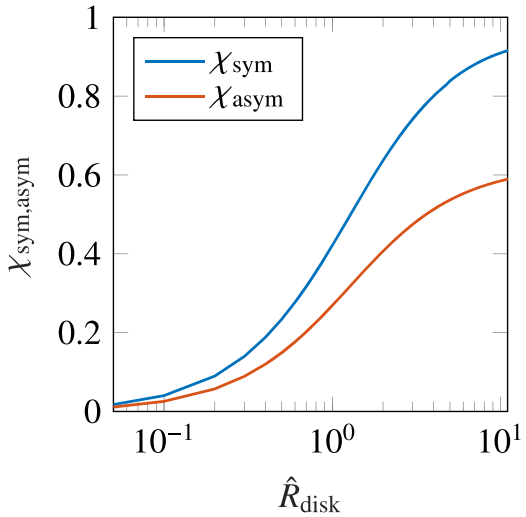

Figure 5. Evolution of χ_{sym} and χ_{asym} as a function of $\hat{R}_{disk}$.

where we have introduced

$$\chi_{sym}(\hat{R}_{disk}) = \frac{\beta_{redep}}{2\pi^2\hat{R}_{disk}^2} \times \int_0^{\hat{R}_{disk}}\int_0^{2\pi}\int_0^{\pi}\int_0^{\hat{R}_{max}} \gamma(r',\,\mu,\,1)\mathrm{d}\hat{r}'\mathrm{d}\varphi'\mathrm{d}\varphi\hat{r}\mathrm{d}\hat{r}$$

and

$$\chi_{asym}(\hat{R}_{disk}) = \frac{\beta_{redep}}{2\pi^2\hat{R}_{disk}^2} \times \int_0^{\hat{R}_{disk}}\int_0^{2\pi}\int_0^{\pi}\sin\varphi'\int_0^{\hat{R}_{max}} \gamma(r',\,\mu,\,1)\mathrm{d}\hat{r}'\mathrm{d}\varphi'\mathrm{d}\varphi\hat{r}\mathrm{d}\hat{r}. \quad (10)$$

χ_{sym} and χ_{asym} describe respectively the isotropic redeposition of impurity and the radial asymmetry of the impurity redeposition in the radial direction. χ_{sym} and χ_{asym} vary slowly with $\hat{R}_{disk}$ (figure 5). The expression (10) was derived assuming $B > 0$, i.e. a magnetic field oriented in the positive toroidal direction as sketched in figure 1, and $\eta_{asym}^{rad} \to -\eta_{asym}^{rad}$ and $\chi_{asym} \to -\chi_{asym}$ when $B < 0$.

Profiles of ξ_{redep} calculated with the expression (9) for tungsten impurities at high (low) electron density and temperature are plotted in figures 6(a) and (b) as a function of the radius R_{disk} of the circular sample. At high plasma temperature and density, the redeposition pattern of tungsten impurities is symmetric ($\eta_{asym}^{rad} \ll 1$), and $\xi_{redep} \approx 2\chi_{sym}$. At low plasma temperature and density, tungsten redeposition is asymmetric in the radial direction and $\chi_{asym} < 0$.

Values of ξ_{redep} calculated with ERO-D3D simulations of tungsten erosion and redeposition from a circular tungsten sample with uniform plasma conditions and a fixed fraction of low-Z carbon impurity in plasma are also shown in figure 6. The good agreement between values of ξ_{redep} simulated with ERO-D3D and values of ξ_{redep} calculated with the expression (9) shows that the reduced model formed by the expressions (3) and (6) can accurately describe the fraction of tungsten impurities redeposited on material sample simulated with ERO-D3D simulations.

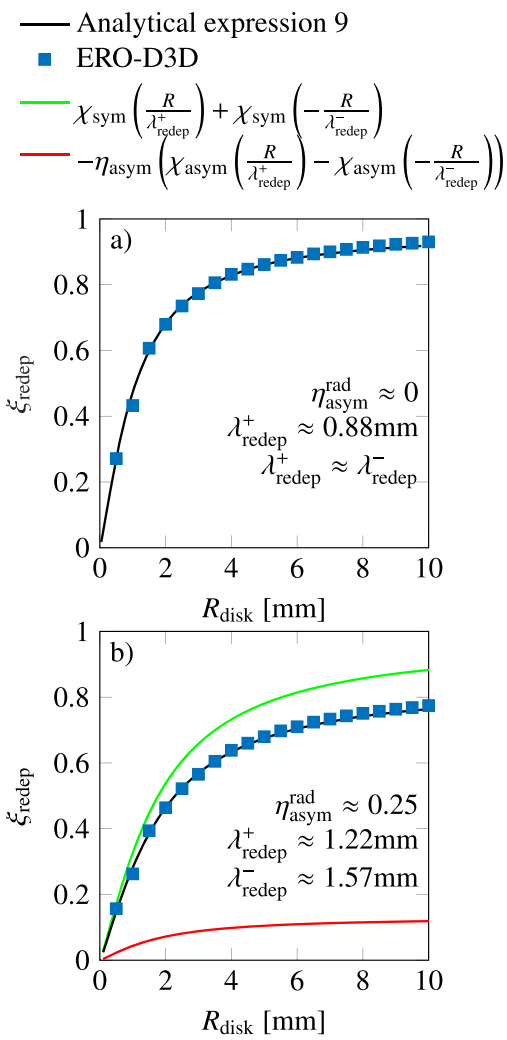

Figure 6. Fraction ξ_{redep} of redeposited tungsten impurities (equation (9)) as a function of the circular tungsten sample radius R_{disk} (black lines) at (a) high plasma density and temperature ($T_e = 35$ eV, $n_e = 10^{14}$ cm^{-3}) and (b) low plasma density and temperature ($T_e = 15$ eV, $n_e = 2 \times 10^{13}$ cm^{-3}). The fraction of redeposited tungsten impurities simulated with ERO-D3D assuming a fixed fraction of carbon impurities in plasma is also shown (blue square).

Due to the slow variation of χ_{sym} and χ_{asym} with $\hat{R}_{disk}$, tungsten redeposition may be still significant when $R_{disk} \approx \lambda^{\pm}_{redep}$, for which $\xi_{redep} \gtrsim 20\%$ (figure 6). Tungsten gross erosion may therefore be accurately inferred from measurements of the tungsten net erosion only on very small tungsten samples. For instance, $\xi_{redep} < 10\%$ for $R_{disk} < 0.2$ mm at high plasma density and temperature.

4.2. Analysis of tungsten erosion and redeposition experiments

The expression (9) of ξ_{redep} and the distribution of redeposited tungsten characterized in the section 3.3 are used in this section to analyze high-Z impurity erosion and redeposition experiments conducted in DIII-D. In these experiments, two circular tungsten samples of different radius were exposed to various attached plasma conditions [14–17]. A detailed description of the plasma conditions and of the experimental

Table 1. Values of Ξ_{ero}^{net} experimentally measured (blue) and calculated with the reduced model formed by the expressions (5), (6) and (9) (green) for tungsten circular samples of radii R_{disk} exposed to various plasma conditions in DIII-D divertor. The parameters of the spatial distribution of redeposited tungsten are calculated assuming $E_{\mathrm{cutoff}} = 1.6T_e$.

Plasma conditions		Experimental net/gross erosion			References	Reduced model (equations (6) and (3))							DIII-D shot number
T_e (eV)	n_e (cm^{-3})	R_{disk} (mm)		$\frac{\Gamma^{\mathrm{net}}_{\mathrm{ero},S_2}}{\Gamma^{\mathrm{net}}_{\mathrm{ero},S_1}}$		λ_{redep} (mm)		$\eta^{\mathrm{rad}}_{\mathrm{asym}}$	β_{redep}	ξ_{redep}		Ξ_{redep}	
		S_1	S_2			$-$	$+$			S_1	S_2		
35	1.2×10^{13}	0.5	5	0.28 (0.33[a])	[14]	1.6	1.6	0	0.93	0.14 (0.14[a])	0.76 (0.69[a])	0.35	#148679-148682
15	1×10^{14}	0.5	7.5	0.17	[17]	0.83	0.82	0.04	0.98	0.30	0.88	0.20	#170843-170847
25	4×10^{13}	0.5	7.5	0.27	[17]	1.1	1.1	0.08	0.96	0.2	0.82	0.25	#170851-170853
26	7.7×10^{12}	0.5	5	0.77 (0.48[a])	[15]	2.26	3.02	0.36	0.76	0.07 (0.07[a])	0.46 (0.53[a])	0.68	#162769-162771
20	4×10^{13}	0.5	5	0.33 (0.34[a])	[16]	1.12	1.24	0.13	0.94	0.18 (20[a])	0.74 (0.75[a])	0.36	#153043-153045

[a] Values indicated in brackets are the ratio obtained from previous comprehensive ERO and REDEP/WBC modeling [15, 16, 23].

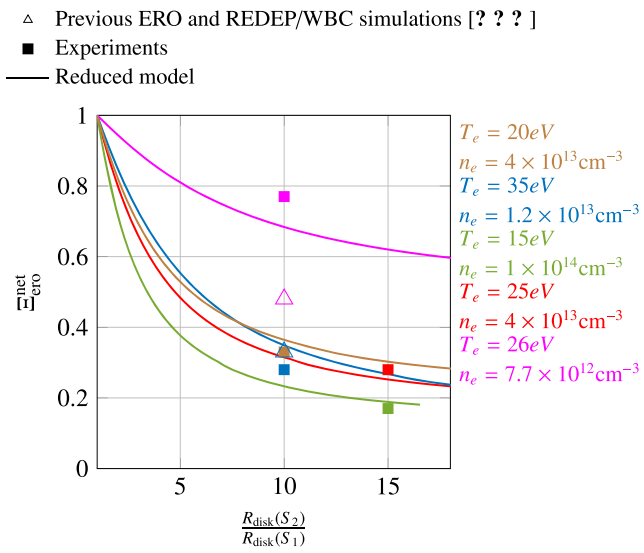

Figure 7. Values of Ξ^{net}_{ero} experimentally measured (square), calculated with the reduced model formed by the expressions (5), (6) and (9) (solid line), and obtained in previous ERO simulations [15, 23] and REDEP/WBC simulations [16] (triangle) as a function of the ratio of the circular tungsten sample radii. Plasma conditions and parameters of the spatial distribution of redeposited tungsten used in the reduced model are reported in table 1. The radius of the smallest sample S_1 is equal to 0.5 mm.

framework is provided in [14–16]. Unpublished experimental measurements [17] were obtained with the plasma conditions described in section 4.1 in [38] using the experimental setup described in [14]. Results of these experiments are summarized in the table 1, where the reported plasma conditions are the radially averaged values of plasma temperature and density above the tungsten samples. These average conditions roughly correspond to the plasma temperature and density at the center of the samples.

Modeling of the net erosion rate experimentally measured from one sample is usually difficult because it requires to model the gross erosion rate of tungsten, which itself requires to model the flux of low-Z impurities impinging on tungsten. Such modeling have been performed by Ding [23] using ERO simulations and by Brooks [16] using REDEP/WBC, with radially varying plasma conditions.

In contrast, modeling the ratio Ξ^{net}_{ero} of the net erosion rates from two samples of different sizes is simpler, as this ratio does not depend on the gross erosion rate when the two samples are exposed to the same plasma conditions (equation (5)). Ξ^{net}_{ero} can be straightforwardly obtained with the reduced model formed by the expression (9) and the spatial distribution of redeposited tungsten characterized by β_{redep}, $\lambda^{\pm}_{redep}$ and η^{rad}_{asym} (equation (6)). Values of Ξ^{net}_{ero} calculated with the reduced model and experimentally measured are displayed in table 1 and in figure 7. The relatively good agreement between calculated and measured values of Ξ^{net}_{ero} indicates that the reduced model might be sufficiently accurate to capture the main features of high-Z impurity redeposition and net erosion in the experimental setup examined in this section.

Nevertheless, no further conclusions should be drawn about the accuracy of this reduced model, since the ability of this model to reproduce values of Ξ^{net}_{ero} for various samples sizes with fixed plasma conditions remains unclear. Further measurements and modeling of Ξ^{net}_{ero} for different sample sizes at given plasma conditions are therefore essential to assess the validity of the reduced model, and thus the subsequent accuracy of the sheath model and ionization rates which effectively govern tungsten net erosion. To that end, enhanced experimental setup are proposed in section 5.

The reduced model introduced in this paper noticeably relies on the assumption that material sample are exposed to sufficiently uniform plasma conditions (section 2.2), whereas non-uniform plasma conditions can be simulated for instance with ERO. The good agreement between the values of Ξ^{net}_{ero} calculated with the reduced model and calculated with ERO [15, 23] or REDEP/WBC [16] (table 1) suggests that the effects of radially non-uniform plasma conditions on high-Z erosion and redeposition may be effectively negligible. The uncertainties due to the radial non-uniformity of plasma temperature and density in the reduced model are briefly discussed below.

4.3. Uncertainties in modeling of high-Z erosion and redeposition due to non-uniform plasma conditions

Plasma conditions in tokamak divertor are usually uniform in the toroidal direction due to the axisymmetry of the tokamak configuration. In contrast, plasma conditions sufficiently uniform in the radial direction are more difficult to obtain. For example, the radial profiles of plasma temperature and density usually vary of at least 30% over a radial distance of 1 cm in DIII-D divertor [14, 16, 23]. It should be noticed that the strike point location in tokamak divertor usually oscillates radially due to the vertical displacement of the plasma and MHD-driven modes. Radial oscillations of the strike point location may spatially average and flatten out the radial profiles of plasma temperature and density above the material samples. The quantification of such effects are out of the scope of this paper.

Radial variations of the plasma conditions across the material samples affect the erosion and redeposition of high-Z impurities through (i) the radial variations of the gross erosion flux and (ii) the radial variations of the spatial distribution of redeposited high-Z impurities.

For instance, effects of non-uniform impurity gross erosion on impurity redeposition and net erosion on a circular sample can be estimated by considering some linear variations of the plasma flux Γ in the radial direction: $\Gamma = \langle\Gamma\rangle\left(1 + \frac{\Delta\Gamma}{\langle\Gamma\rangle}\frac{\hat{r}\sin\varphi}{\hat{R}_{disk}}\right)$. Effects of radially non-uniform gross erosion flux on the fraction ξ_{redep} of redeposited high-Z

impurity are thus of the order of

$$\frac{\Delta\xi_{\mathrm{redep}}}{\xi_{\mathrm{redep}}} = \frac{\Delta\Gamma}{\langle\Gamma\rangle\hat{R}_{\mathrm{disk}}} \times \frac{\int_0^{\hat{R}_{\mathrm{disk}}}\int_0^{2\pi}\int_0^{2\pi}\int_0^{\hat{R}_{\mathrm{max}}}\hat{f}_{\mathrm{redep}}(\hat{r}',\varphi')\sin\varphi\mathrm{d}\hat{r}'\mathrm{d}\varphi'\mathrm{d}\varphi\hat{r}^2\mathrm{d}\hat{r}}{\int_0^{\hat{R}_{\mathrm{disk}}}\int_0^{2\pi}\int_0^{2\pi}\int_0^{\hat{R}_{\mathrm{max}}}\hat{f}_{\mathrm{redep}}(\hat{r}',\varphi')\mathrm{d}\hat{r}'\mathrm{d}\varphi'\varphi\hat{r}\mathrm{d}\hat{r}}. \quad (11)$$

The expression (11) shows that effects of non-uniform plasma and high-Z impurity gross erosion fluxes on ξ_{redep} are negligible when the high-Z impurity redeposition is radially symmetric ($\lambda^{-}_{\mathrm{redep}} \approx \lambda^{+}_{\mathrm{redep}}$). A similar conclusion holds for the effects of radially non-uniform plasma temperature, which induces radially non-uniform sputtering of high-Z impurity, on ξ_{redep}. When the spatial distribution of redeposited impurity is radially asymmetric, radially non-uniform plasma conditions may therefore limit the accuracy of the reduced model by inducing radially non-uniform impurity gross erosion.

Effects of the radial variations of the spatial distribution of redeposited high-Z impurities due to radially non-uniform plasma conditions on impurity redeposition is difficult to quantify due to the nonlinear dependency of $\hat{f}_{\mathrm{redep}}$ on $\lambda^{\pm}_{\mathrm{redep}}$. However, the slow variation of χ_{sym} and χ_{asym} with $\hat{R}_{\mathrm{disk}}$ (figure 5) indicates that ξ_{redep} slowly varies with $\lambda^{\pm}_{\mathrm{redep}}$. Moreover, variations of $\lambda^{\pm}_{\mathrm{redep}}$ and β_{redep} with the plasma conditions are small when the plasma density is high enough. For tungsten, $\lambda^{\pm}_{\mathrm{redep}}$ and β_{redep} weakly vary with n_e and T_e when $n_e \gtrsim 5 \times 10^{13}\,\mathrm{cm}^{-3}$ (figure 4).

Noticing that the radial symmetry of the distribution of redeposited tungsten impurities decreases as the plasma density increases (figures 4(b), (e) and (h)), uncertainties in the reduced model formed by the expressions (9) and (6) due to radially non-uniform plasma conditions thus largely diminish when tungsten samples are exposed to plasma at high density. Similar conclusions can be drawn when considering toroidal asymmetry, for instance due to toroidally non-uniform flux of low-Z impurity impigning on tungsten samples.

Finally, uncertainties in modeling of erosion and redeposition experiments diminish in general as the radial size of the high-Z material samples decreases. The size and the shape of the material can be therefore chosen to minimize the effects of non-uniform plasma conditions on high-Z impurity redeposition in tokamak divertor, as discussed in the next section.

5. Optimizing the shape and the size of the material samples to improve the experimental characterization of high-Z net erosion and redeposition

Circular tungsten samples of various radii were exposed in DIII-D experiments using DiMES [12, 14–16]. Other sample geometries may be however considered, for instance rectangular shapes. Such geometries can provide additional geometrical parameters which affect the fraction of redeposited impurities and which can be varied between experiments. In DIII-D experiments, material samples must be designed to be embedded on the DiMES head, which is a disk of radius 2.5 cm [14]. With this constraint, some enhanced experimental setup are proposed in this section to improve the experimental assessment of net erosion and redeposition of high-Z impurities.

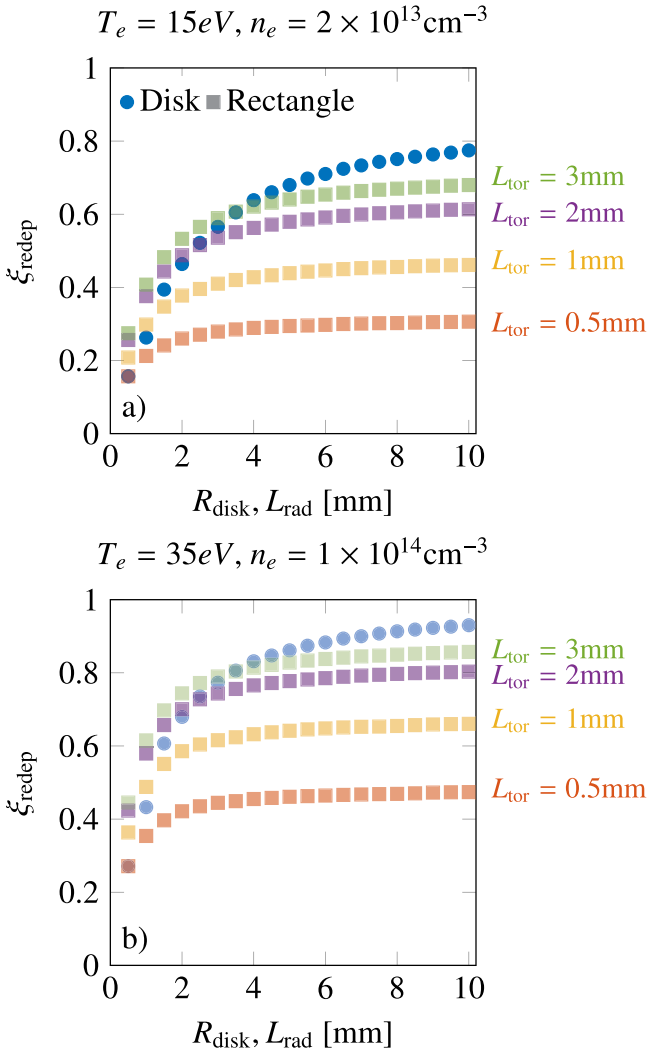

Figure 8. Fraction ξ_{redep} of tungsten eroded and redeposited on a circular sample (circle mark) and rectangular sample (square marks) as a function of the radial width of the sample calculated with the reduced model formed by the expressions (6) and (3) for low (a) and high (b) plasma temperature and density.

5.1. Circular vs rectangular shape

A rectangular material sample aligned with the magnetic field line is characterized by its toroidal width L_{tor} and its radial width L_{rad} (figure 2). The fraction of high-Z impurities eroded and redeposited on such rectangular sample varies with L_{tor} and L_{rad}, as shown in the figure 8. As pointed out in the previous section, plasma conditions which are sufficiently radially uniform across the material sample are difficult to generate in tokamak divertor. This limitation can be overcome with a rectangular shape by varying L_{tor}, while keeping L_{rad}

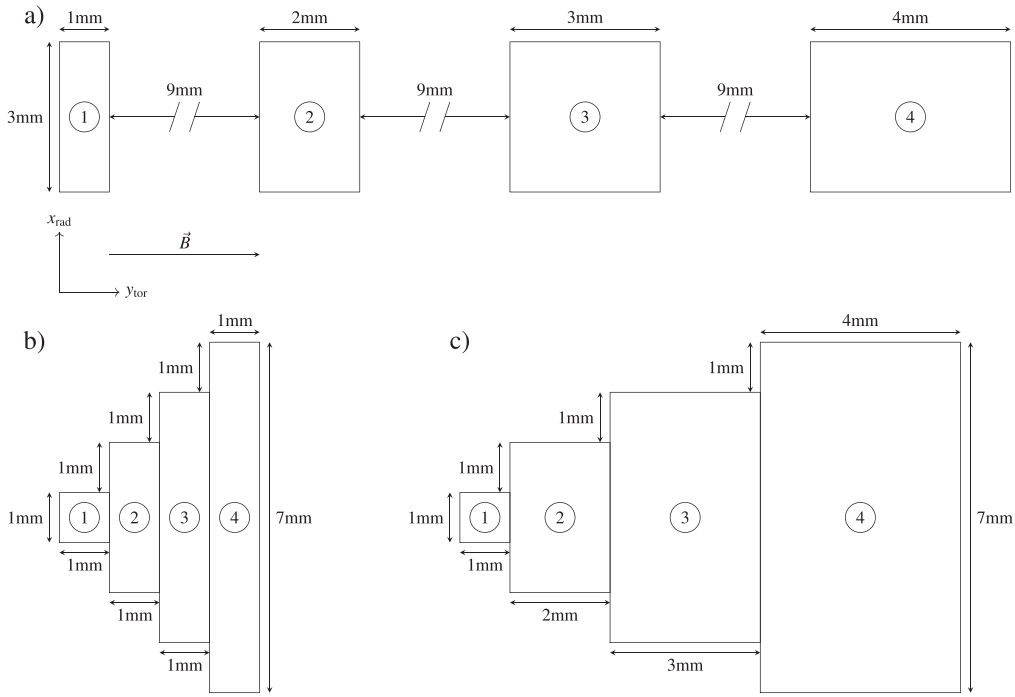

Figure 9. Advanced geometries combining four rectangular material samples to measure high-Z impurities net erosion as a function of the region defined by each rectangular sample. These regions are labeled ①, ②, ③ and ④.

constant and as small as possible. For instance, the figure 8 indicates that the fraction of redeposited tungsten on a rectangular sample significantly varies with L_{tor} when $L_{rad} \gtrsim 3$ mm.

These results are also valid for an elliptic sample of semi-minor axis L_{rad} and semi-major axis L_{tor}.

5.2. Advanced geometries

As mentioned in the section 4.2, measuring Ξ_{ero}^{net} for various sizes of material sample with fixed plasma conditions is critical to thoroughly validate models predicting high-Z impurity redeposition and net erosion. However, available experimental time in tokamaks like DIII-D is usually limited, and experiments must be designed to collect experimental data during a limited number of plasma shots. Considering the previously described rectangular samples, we propose hereby three geometries to measure tungsten net erosion during a single plasma shot as a function of a well-defined geometrical parameter (figure 9). These experimental setups combine four rectangular tungsten samples of various radial and toroidal widths aligned with the magnetic field. The aforementioned geometrical parameter is in this case the areas defined by each rectangular sample, and labeled ①, ②, ③ and ④.

The setup plotted in figure 9(a) consists in four rectangular samples of fixed radial width but increasing toroidal width. Samples are toroidally distant from each other by a distance of 9 mm. Within this configuration, redeposition of tungsten impurities from one sample onto another one is negligible, since the radial distribution of tungsten impurities is close to zero around 9 mm–1 cm (see e.g. figures 3(b) and (e)).

The fraction ξ_{redep} of redeposited tungsten in each region and the ratio Ξ_{ero}^{net} of the net erosion rate from each region over the net erosion rate from the region ① are plotted in figure 10. Variations of Ξ_{ero}^{net} are significant as the toroidal width of the sample increases, and should be thus experimentally measurable. It should be noticed that variations of Ξ_{ero}^{net} are more pronounced as the radial width of the samples increases. This radial width—here arbitrarily taken equal to 3 mm—is only limited by the radial scale length of the plasma conditions, and can be reduced or increased depending on those plasma conditions.

Larger variations of Ξ_{ero}^{net} can also be obtained by considering samples of various radial width and fixed toroidal width (figure 9(b)), or samples of various radial and toroidal widths (figure 9(c)). As shown in figure 10, the variations of Ξ_{ero}^{net} are more significant when the toroidal width of the sample is increased with the radial width, as the sample areas are larger. The experimental setup sketched in figure 9(c) is thus more robust against experimental uncertainties.

The geometries proposed in figures 9(a) and (c) are therefore two examples of experimental setup which can provide enhanced experimental characterization of net erosion —and thus redeposition—of high-Z impurities during a single plasma shot. It should be noticed that the analysis of tungsten redeposition presented for those geometries could be performed on virtually any material sample by arbitrarily defining several redeposition regions of various size and/or shape on this sample. Redeposition regions defined by rectangular samples, as the ones used in the experimental setup presented in this section, are however easier to distinguish than a plain tungsten rectangular sample during the post-mortem analysis of material samples.

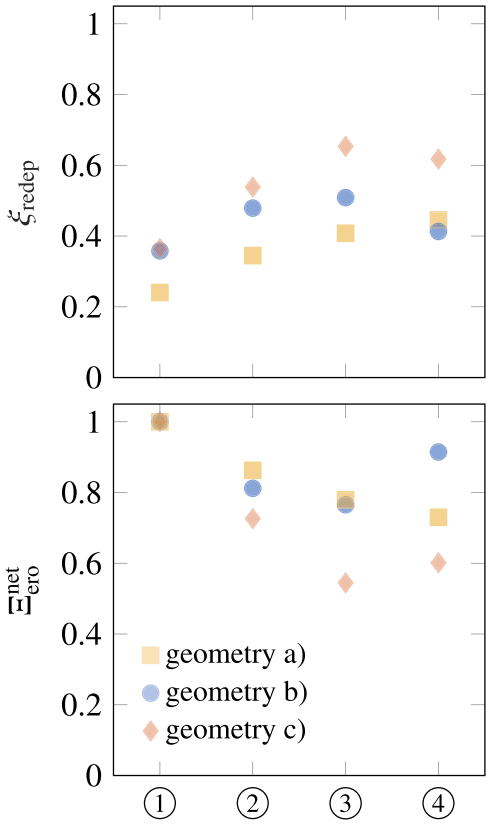

Figure 10. Values of ξ_{redep} and Ξ^{net}_{ero} (see section 2.1) calculated for tungsten with the reduced model formed by the expressions (3) and (6) for the regions ①, ②, ③ and ④ of the geometries sketched in figure 9. Ξ^{net}_{ero} is here the ratio of the net erosion rate from each region over the net erosion rate from the region ①.

6. Summary

High-Z impurity erosion in tokamak divertor results from various complex physics processes (material sputtering, impurity ionization, impurity motion in electric sheath,…). While material gross erosion can be measured *in situ* in tokamak divertor (e.g. spectroscopically), material net erosion is usually inferred from postmortem analysis of PFCs. The interpretation and the modeling of high-Z impurities erosion and redeposition experiments in tokamak divertor is therefore complex. Furthermore, first principle modeling and experimental measurements of key processes governing erosion and redeposition of high-Z impurities in divertor, such as the structure of the electric sheath and the ionization rates of neutral and low charge state tungsten impurities, are extremely challenging.

Stangeby, Rudakov and Brooks have introduced a original experimental setup in DIII-D, where two high-Z material samples of different sizes were exposed to the same attached plasma conditions in the DIII-D divertor, to obtain a well constrained experimental measurement of high-Z material net erosion. The analysis and the interpretation of these experiments can be however cumbersome, as the modeling of these experiments with Monte-Carlo impurity erosion and transport model (e.g. ERO) includes a large number of parameters.

To overcome this issue, a reduced model of high-Z impurities erosion and redeposition is introduced. This model relies on the assumption that plasma conditions are sufficiently uniform above the material samples in both toroidal and radial direction. Within this assumption, the spatial distribution of redeposited high-Z impurities can be well approximated by an analytical distribution characterized by only a few parameters (equation (6)). The fraction of high-Z impurities eroding and redepositing on a material sample is then obtained from the integral of the distribution of impurities redeposited onto the material sample (equation (3)).

This reduced model is applied to analyze recent experiments on tungsten erosion and redeposition conducted in DIII-D, in which several circular tungsten samples of various radii were exposed to single attached plasma conditions. Net erosion rates corresponding to these plasma conditions were measured through postmorterm analysis of the tungsten samples. The ratio of the net erosion rates obtained from two samples of different size exposed to the same plasma conditions calculated with the reduced model are in agreement with the experimental values.

Additional experiments are nevertheless required to further assess the ability of this reduced model to consistently predict the ratio of the net erosion rates from tungsten samples of various sizes exposed to several plasma conditions. This assessment is critical to determine the validity of the underlaying models describing key processes governing tungsten redeposition and net erosion, such as the structure of the electric sheath and the ionization rates of neutral and low charge state tungsten impurities, which largely determine the amount of tungsten effectively emitted in the scrape-off layer plasma. To that end, several enhanced experimental setups are finally proposed to measure and compare net erosion rates from samples of various areas during a single plasma experiment in tokamak divertor. Uncertainties in parameters governing tungsten prompt redeposition and thus affecting tungsten erosion in tokamak divertor, such as ionization rates and sheath scale length, will be discussed elsewhere.

Acknowledgments

This material is based upon work supported by the U.S. Department of Energy, Office of Science, Office of Fusion Energy Sciences, using the DIII-D National Fusion Facility, a DOE Office of Science user facility, under Awards DE-SC0018423, DE-FC02-04ER54698, DE-FG02-07ER54917 and DE-NA0003525. DIII-D data shown in this paper can be obtained in digital format by following the links at https://fusion.gat.com/global/D3D_DMP.

Disclaimer

This report was prepared as an account of work sponsored by an agency of the United States Government. Neither the United States Government nor any agency thereof, nor any of their employees, makes any warranty, express or implied, or

assumes any legal liability or responsibility for the accuracy, completeness, or usefulness of any information, apparatus, product, or process disclosed, or represents that its use would not infringe privately owned rights. Reference herein to any specific commercial product, process, or service by trade name, trademark, manufacturer, or otherwise does not necessarily constitute or imply its endorsement, recommendation, or favoring by the United States Government or any agency thereof. The views and opinions of authors expressed herein do not necessarily state or reflect those of the United States Government or any agency thereof.

ORCID iDs

J Guterl https://orcid.org/0000-0002-1049-3094
W R Wampler https://orcid.org/0000-0002-4263-252X
D Rudakov https://orcid.org/0000-0002-5266-4269
P Snyder https://orcid.org/0000-0002-0613-4232

Q2 ## References

[1] Behrisch R, Federici G, Kukushkin A and Reiter D 2003 Material erosion at the vessel walls of future fusion devices *J. Nucl. Mater.* **313–316** 388–92
[2] Philipps V 2011 Tungsten as material for plasma-facing
Q3 components in fusion devices *J. Nucl. Mater.* **415**
[3] Brezinsek S 2015 Plasma-surface interaction in the Be/W environment: conclusions drawn from the JET-ILW for ITER *J. Nucl. Mater.* **463** 11–21
[4] Pitts R *et al* 2013 A full tungsten divertor for iter: physics issues and design status *J. Nucl. Mater.* **438** S48–56
[5] van Rooij G *et al* 2013 Tungsten divertor erosion in all metal devices: lessons from the ITER like wall of JET *J. Nucl. Mater.* **438** S42–7
[6] Hakola A *et al* 2016 Gross and net erosion of tungsten in the outer strike-point region of ASDEX Upgrade *Phys. Scr.* **T167** 014026
[7] Abrams T *et al* 2017 The inter-ELM tungsten erosion profile in DIII-D H-mode discharges and benchmarking with ERO +OEDGE modeling *Nucl. Fusion* **57** 056034
[8] Mayer M, Rohde V, Ramos G, Vainonen-Ahlgren E, Likonen J and Chen J L 2007 Erosion of tungsten and carbon markers in the outer divertor of ASDEX-Upgrade *Phys. Scr.* **T128** 106–10
[9] Mayer M, Likonen J, Coad J P, Maier H, Balden M, Lindig S, Vainonen-Ahlgren E and Philipps V 2007b Tungsten erosion in the outer divertor of JET *J. Nucl. Mater.* **363–365** 101–6
[10] Ding R *et al* 2015 Material migration studies with an ITER first wall panel proxy on EAST *Nucl. Fusion* **55** 023013
[11] Catarino N, Barradas N, Corregidor V, Widdowson A, Baron-Wiechec A, Coad J, Heinola K, Rubel M and Alves E 2017 Assessment of erosion, deposition and fuel retention in the JET-ILW divertor from ion beam analysis data *Nucl. Mater. Energy* **12** 559–63
[12] Stangeby P *et al* 2013 An experimental comparison of gross and net erosion of mo in the DIII-d divertor *J. Nucl. Mater.* **438** S309–12
[13] Wampler W, Stangeby P, Watkins J, Buchenauer D, Rudakov D and Wong C 2013 Measurements of net erosion and redeposition of molybdenum in DIII-d *J. Nucl. Mater.* **438** S822–6
[14] Rudakov D L *et al* 2014 Net versus gross erosion of high-Z materials in the divertor of DIII-D *Phys. Scr.* **T159** 014030
[15] Ding R *et al* 2017 High-Z material erosion and its control in DIII-d carbon divertor *Nucl. Mater. Energy* **12** 247–52
[16] Brooks J, Elder J, McLean A, Rudakov D, Stangeby P and Wampler W 2015 Analysis of a tungsten sputtering experiment in DIII-d and code/data validation of high redeposition/reduced erosion *Fusion Eng. Des.* **94** 67–71
[17] Wampler W R 2018 Private communication
[18] Wong C, Whyte D, Bastasz R, Brooks J, West W and Wampler W 1998 Divertor materials evaluation system (DiMES) *J. Nucl. Mater.* **258–263** 433–9
[19] Rudakov D L *et al* 2009 Overview of the recent DiMES and MiMES experiments in DIII-d *Phys. Scr.* **T138** 014007
[20] Brooks J N 1990 Near-surface sputtered particle transport for an oblique incidence magnetic field plasma *Phys. Fluids* B **2** 1858–63
[21] Tskhakaya D and Groth M 2015 Modelling of tungsten re-deposition coefficient *J. Nucl. Mater.* **463** 624–8
[22] Ding R *et al* 2017 Advances in understanding of high-Z material erosion and re-deposition in low-Z wall environment in DIII-D *Nucl. Fusion* **57** 056016
[23] Ding R *et al* 2015 Simulation of gross and net erosion of high-Z materials in the DIII-D divertor *Nucl. Fusion* **56** 016021
[24] Chodura R 1982 Plasma–wall transition in an oblique magnetic field *Phys. Fluids* **25** 1628
[25] Coulette D and Manfredi G 2016 Kinetic simulations of the Chodura and Debye sheaths for magnetic fields with grazing incidence *Plasma Phys. Control. Fusion* **58** 025008
[26] Smyth R T, Ballance C P, Ramsbottom C A, Johnson C A, Ennis D A and Loch S D 2018 Dirac r-matrix calculations for the electron-impact excitation of neutral tungsten providing noninvasive diagnostics for magnetic confinement fusion *Phys. Rev.* A **97**
[27] Fussman G (ed) 1995 *IAEA Proc. 15th Int. Conf. on Plasma Physics and Controlled Nuclear Fusion Research* vol 2 (Vienna: IAEA) p 145
[28] Chankin A V, Coster D and Dux R 2014 Monte Carlo simulations of tungsten redeposition at the divertor target *Plasma Phys. Control. Fusion* **56** 025003
[29] Cohen R H and Ryutov D D 1998 Particle trajectories in a sheath in a strongly tilted magnetic field *Phys. Plasmas* **5** 808–17
[30] Guterl J, Abrams T, Johnson C A, Jaervinen H Q and Wang A 2019 ERO modeling and analysis of tungsten erosion and migration from a toroidally symmetric source in DIII-D divertor *Nucl. Fusion* Accepted (https://doi.org/10.1088/ Q4
1741-4326/ab4c54)
[31] Ryutov D D 1996 Kinetic theory analysis of sheaths and shocks *Contrib. Plasma Phys.* **36** 207–19
[32] Thompson M W 1968 II. The energy spectrum of ejected atoms during the high energy sputtering of gold *Phil. Mag.* **18** 377–414
[33] Möller W, Eckstein W and Biersack J 1988 Tridyn-binary collision simulation of atomic collisions and dynamic composition changes in solids *Comput. Phys. Commun.* **51** 355–68
[34] Summers H P 2004 The ADAS User Manual version 2.6 Q5
http://adas.ac.uk
[35] Kirschner A, Philipps V, Winter J and Kögler U 2000 Simulation of the plasma-wall interaction in a tokamak with the Monte Carlo code ERO-TEXTOR *Nucl. Fusion* **40** 989–1001
[36] Kogler U and Winter J 1997 ERO-TEXTOR: 3D Monte-Carlo Q6
code for local impurity modeling in the scrape-off layer of TEXTOR *Technical Report, Julich Report*
[37] Mousel T, Eckstein W and Gnaser H 1999 Energy spectra of sputtered species under sub-keV ion bombardment:

experiments and computer simulations *Nucl. Instrum. Methods Phys. Res.* B **152** 36–48

[38] Abrams T *et al* 2018 Experimental validation of a model for particle recycling and tungsten erosion during ELMs in the DIII-d divertor *Nucl. Mater. Energy* **17** 164–73